Lawrence Berkeley Laboratory
UNIVERSITY OF CALIFORNIA

Physics Division

Submitted to Astrophysical Journal

A Measurement of the Temperature of the Cosmic Microwave Background at a Frequency of 7.5 GHz

A. Kogut, M. Bensadoun, G. De Amici, S. Levin,
G.F. Smoot, and C. Witebsky

June 1989

Prepared for the U.S. Department of Energy under Contract Number DE-AC03-76SF00098.

A MEASUREMENT OF THE TEMPERATURE OF THE COSMIC MICROWAVE BACKGROUND AT A FREQUENCY OF 7.5 GHZ

A. KOGUT, M. BENSADOUN, G. DE AMICI, S. LEVIN, G.F. SMOOT, AND C. WITEBSKY
Lawrence Berkeley Laboratory and Space Sciences Laboratory
University of California

ABSTRACT

We have measured the intensity of the cosmic microwave background (CMB) at a frequency of 7.5 GHz (wavelength 4.0 cm) using a ground-based, total power radiometer calibrated at the horn aperture by an external cryogenic reference target. The radiometer measured the difference in antenna temperature between the reference target and the zenith sky from a dry, high-altitude site. Subtraction of foreground signals (primarily atmospheric and galactic emission) measured with the same instrument leaves the CMB as the residual. The radiometer measured the atmospheric antenna temperature by correlating the signal change with the airmass in the beam during tip scans. The small galactic signal was subtracted based on extrapolation from lower frequencies, and was checked by differential drift scans. The limiting uncertainty in the CMB measurement was the effect of ground radiation in the antenna sidelobes during atmospheric measurements. The thermodynamic temperature of the CMB at 7.5 GHz is 2.59 ± 0.07 K (68% confidence level).

Subject headings: cosmic background radiation, csomology

I. INTRODUCTION

The cosmic microwave background (CMB) is widely interpreted as a relic of a hot, dense phase in the early universe. Radiative processes at redshifts greater than $z_{obs} \sim 2.2 \times 10^6 \, \Omega_b^{-1/3} \, h^{-2/3}$ efficiently thermalize an arbitrary initial CMB spectrum to a Planck spectrum (Danese and De Zotti 1982), where Ω_b is the baryon density relative to the closure density and h is the Hubble constant in units of 50 km s^{-1} Mpc^{-1}. Energy releases to the matter or radiation fields at epochs more recent than z_{obs} will distort the CMB spectrum from a Planckian distribution, with the size and shape of the distortion dependent on the details and epoch of the energy release.

Matsumoto *et al.* (1988) report such a distortion at sub-mm wavelengths. The excess flux has been variously interpreted in terms of Compton distortions or dust emission from an early generation of stars (e.g., Hayakawa *et al.* 1988, Adams *et al.* 1989 and references therein). The CMB spectrum in the Rayleigh-Jeans region ($\lambda > 1$ cm) can distinguish between competing models for the sub-mm excess. In addition, the long-wavelength spectrum may contain distortions unrelated to the apparent excess in the Wien region.

As part of an on-going effort to characterize the Rayleigh-Jeans CMB spectrum, we have measured the CMB intensity at a number of frequencies from a high-altitude site (Smoot *et al.* 1987, 1985). Our results limited potential energy releases to $\delta E/E \leq 1\%$ at redshifts between z_{obs} and $\sim 4 \times 10^4$ (Smoot *et al.* 1988). Ground-based results, however, differed from measurements using other techniques (e.g., Johnson and Wilkinson 1986, Crane *et al.* 1986). In an effort to alter and reduce potential systematics common to recent ground-based results, we returned to our high-altitude site in late summer 1988 with a new cryogenic reference target, improved instruments at 1.5 and 3.8 GHz, and a new radiometer operating at 7.5 GHz (Smoot *et al.* 1989). This paper details the measurement at 7.5 GHz.

II. CONCEPT OF THE MEASUREMENT

We measure the CMB spectrum with a radiometer, a device whose output voltage is proportional to the microwave power per unit bandwidth intercepted by the input port. In the Rayleigh-Jeans region, signals are commonly quoted in units of antenna temperature

T_A, related to the power emitted by a blackbody completely filling the antenna aperture by the relation

$$T_A = \frac{P}{kB} = \frac{x}{e^x - 1} T, \quad (1)$$

where P is the received power, k is Boltzmann's constant, B is the bandwidth of the observation, T is thermodynamic temperature, and x is the dimensionless frequency

$$x = \frac{h\nu}{kT}.$$

Here h is Planck's constant and ν is the frequency. The experiment compares the output voltage as the radiometer alternately views the zenith sky and a cryogenic reference target with a well-determined antenna temperature. The antenna temperature of the zenith sky, $T_{A,zenith}$, is then determined by the voltage difference and the calibration constant G of the radiometer,

$$T_{A,zenith} - T_{A,load} = G(S_{zenith} - S_{load}), \quad (2)$$

where $T_{A,load}$ is the antenna temperature of the reference target, and S_{zenith} and S_{load} refer to the output voltage as the radiometer views the zenith and the reference load, respectively. The zenith antenna temperature is the sum of many signals:

$$T_{A,zenith} = T_{A,CMB} + T_{A,Atm} + T_{A,Gal} + T_{A,Ground} + T_{A,RFI} + \Delta T_{Offset}, \quad (3)$$

where $T_{A,CMB}$ is the antenna temperature of the CMB, $T_{A,Atm}$ is the antenna temperature of the atmosphere, $T_{A,Gal}$ is the antenna temperature of the Galaxy, $T_{A,Ground}$ is the antenna temperature of the Earth seen in the antenna sidelobes, $T_{A,RFI}$ is the antenna temperature of man-made radio-frequency interference (RFI), and ΔT_{Offset} refers to any systematic change in radiometer performance in the interval between viewing the zenith and the cold load. Radiation from the sun and moon is easily avoided by observing only when these sources are below the horizon. Equations 2 and 3 can be solved for the CMB temperature:

$$T_{A,CMB} = G(S_{zenith} - S_{load}) + T_{A,load} - T_{A,Atm} - T_{A,Gal} - T_{A,ground} - T_{A,RFI} - \Delta T_{Offset}. \quad (4)$$

We calculated $T_{A,load}$ based on the known and measured properties of the materials used in the reference target; to first order, it is simply the boiling temperature of the liquid

helium (LHe) cryogen. We measured directly all other terms in Eq. 4 using the same instrument as for the zenith sky measurement. Tipping the radiometer a fixed amount and correlating the increased signal with the increased airmass in the beam measured the atmospheric antenna temperature. The minor galactic contribution is estimated from extrapolations of maps at lower frequencies, and checked by differential drift scans. We estimated $T_{A,ground}$ based on the measured far-field beam pattern and on tests that modulated the temperature of the radiation in the antenna sidelobes.

We performed the measurements from the Nello Pace Laboratory of the University of California's White Mountain Research Station. The station is located on a high mountain plateau (elevation 3800 m) in the rain shadow of the Sierra Nevada range in eastern California (latitude 37.5° N). Typical column densities of precipitable water vapor during clear summer nights are in the range 2—5 mm. The magnitude and variability of the atmospheric signal from the Laboratory are approximately a factor of three smaller than from sea level in Berkeley. The station is also remote from man-made radio sources, which precluded operation of the instrument near major population centers.

III. DESCRIPTION OF THE INSTRUMENT

a) The Radiometer

The radiometer is a direct-gain, total-power receiver with a corrugated conical horn antenna on the input port. The RF chain is shown in Figure 1. The antenna is the same one used for measurements at 10 GHz (Kogut *et al.* 1988) with a new circular-to-rectangular waveguide transition optimized for operation at 7.5 GHz. A short rectangular waveguide ended in a transition to semi-rigid stainless-steel SMA coaxial cable. The signal from the input underwent 40 dB of RF amplification in the first stage amplifier with a nominal 7.25—7.75 GHz bandpass and an isolator on the input to prevent impedance-dependent offset changes. A second RF amplifier provided an additional 25 dB of gain. A Schottky-barrier diode rectified the amplified RF signal. Attenuation of 6 dB between the two amplifiers and 13 dB between the second amplifier and the detector diode served to reduce reflections among the RF components. The signal from the diode underwent an additional amplification of 2500 in a DC amplifier, which integrated the signal for a period of 2 seconds. The amplified DC signal was digitized and recorded every two seconds by the same multiplexer/ADC used by the 10 GHz radiometer in previous years (Kogut *et al.*

1988). The 7.5 GHz radiometer shared the system in 1988 with radiometers operating at frequencies of 1.5, 3.8, and 90 GHz. Table 1 summarizes the properties of the radiometer.

The radiometer performed atmospheric measurements from a small cart while suspended from pivots rigidly attached to its outer shell. A bar attached to the bottom of the radiometer connected to a series of pegs and allowed the radiometer to view fixed zenith angles of nominal values ±40°, ±30°, ±15°, and 0° (zenith). We aligned the cart E-W so that negative angles had azimuth 270±1° (due west) while positive angles had azimuth 90±1° (due east). An electronic clinometer indicated the zenith angle of the radiometer. The radiometer performed differential galactic drift scans from its cart or from a turntable that rotated to allow the radiometer to view two positions at constant zenith angle (15°) separated by 180° in azimuth.

b) The Reference Target

The largest term in Eq. 4 is the antenna temperature of the reference load, $T_{A,load}$. Between 1987 and 1988 we built a new reference target optimized for use between 1 and 10 GHz (Figure 2). It consisted of a microwave absorber (Emerson & Cummings EHP-12 backed by E&C LS) submerged in LHe within a large (81 cm diameter) upright (162 cm tall) cryostat. A metalized plastic cylinder surrounded the absorber and acted as an oversized multi-mode waveguide ("radiometric wall") to ensure that the absorber filled the antenna aperture while minimizing emission from warm portions of the cryostat. Thin (13 μm) polyethylene windows at the top of the cryostat prevented air from condensing on the radiometric wall and adding to its emissivity. A fraction of the helium boil-off gas, heated above ambient temperature, circulated between the polyethylene windows to prevent the formation of water condensation or frost on the top window. Two thin (76 and 175 μm) teflon-impregnated glass cloth (Fluorglas 381-3) windows served as low-pass filters, blocking the infrared (IR) heat leak to the microwave absorber. Although the windows had large absorption in the IR, they were essentially transparent below 10 GHz (opacity $\tau \leq 2 \times 10^{-4}$ at 7.5 GHz). Located in the radiometric space between the absorber and the upper windows, the Fluorglas windows intercepted IR radiation and warmed the LHe boiloff gas.

Although similar to the reference load used in previous years, the new cold load incorporated several important changes. The Fluorglas windows replaced a cumbersome

shutter. The new absorber was 50% thicker, and the radiometric wall slightly wider in diameter. The transition from the top flange to the aluminized fiberglass radiometric wall was simplified and made smoother, with no steps or gaps larger than 0.5 mm. A series of sensors behind the radiometric wall allowed better estimation of the cryogen level and the temperature profile in the radiometric wall.

We have extensively modelled and tested the radiometric properties of the cold load (Appendix A). To lowest order, the antenna temperature of the reference target is simply the thermodynamic temperature of the cryogen converted to antenna temperature. Given knowledge of the positions, reflectivity, and emissivity of the material between the radiometer and the absorber, contributions to $T_{A,load}$ arising from reflected and emitted radiation can be calculated. At 7.5 GHz, these corrections are all small (< 20 mK). The largest single correction is the power reflected from the Fluorglas windows, estimated at 6 mK for the two windows. The largest corrections for emission from sources other than the absorber are estimated at 6 mK for emission from the Fluorglas windows and 6 mK emission from joints in the radiometric wall. Other sources of emission or reflection are smaller still.

The barometric pressure at White Mountain in 1988 was 481±1 mm Hg, somewhat lower than in previous years. This corresponded to a LHe boiling point of 3.771±0.002 K (Donnelly 1967). The contributions to $T_{A,load}$ are summarized in Appendix A. We took the antenna temperature of the reference target in 1988 to be $T_{A,load} = 3.613 \pm 0.009$ K.

c) Ambient Target

We calibrated the radiometer by comparing the voltage difference as the radiometer viewed two known, dissimilar targets: the cryogenic reference target and a small ambient target. The ambient target consisted of a slab of microwave absorber (Eccosorb CV-3) 25 cm x 25 cm x 8 cm, enclosed in a metal box insulated by 2.5 cm of closed-cell foam. The target could be opened to cover the antenna aperture completely, and was otherwise left closed to allow the interior to thermalize. A thermistor within the Eccosorb monitored the target temperature.

d) Ground Shield

We measured the antenna to have a half-power beam width of 20±2° at 7.5 GHz. We built a large pyramidal ground shield that attached to the radiometer during atmospheric scans and the measurement of $T_{A,zenith}$. The height and position of the shield were such that angles smaller than 35° viewed the sky directly, while larger beam angles reflected from the shield. A flared section with flare radius of two wavelengths reduced diffraction over the edges of the shield. The far-field beam pattern of the corrugated horn antenna is shown in Figure 3. The contribution of the ground shield can be seen at beam angles >35°, where the shield added between 10 and 20 dB additional rejection of the ground signal.

IV. SYSTEM PERFORMANCE TESTS

We performed numerous tests on site at White Mountain to assess the magnitude of effects contributing to the error budget of the measurement.

a) Systematic Changes

The entire experiment depended upon the radiometer's response remaining independent of its orientation. We tested extensively to place limits on this effect. In the simplest test, we clamped the ambient calibration target firmly over the antenna aperture, then repeatedly changed the radiometer's position while recording the output. The positions were either those of the zenith sky measurement (up and down) or those of an atmospheric measurement (-40°, -30°, zenith, +30°, and +40°). We used the signal-averaged data to search for systematic signal changes correlated with position.

The radiometer may be modelled as an ideal radiometer with a system temperature T_{system}, power absorption coefficient A, and power reflection coefficient R, observing a target at temperature T_{Target}. Neglecting terms second-order in A and R, the output voltage is

$$S = \frac{1}{G}\{ T_{Target} + T_{system} + R(T_{system} - T_{Target}) + A(T_{int} - T_{Target}) \}, \qquad (5)$$

where T_{int} is the temperature of the internal absorbing component. Coherent reflection effects have been ignored. Changes in the calibration constant G, the system temperature, or the reflection or absorption coefficients will produce a voltage change, which will be detected if it is systematically correlated with radiometer position.

These tests were sensitive to changes in radiometer calibration constant or system temperature, but were not particularly sensitive to changes in insertion loss or reflection coefficient of the components in the RF chain. To test for these effects, the radiometer must view a target with temperature significantly different from the system temperature and the temperature of the RF components. For this purpose we used a small liquid nitrogen (LN) target, which consisted of a disk of microwave absorber (Eccosorb CV-3 backed by two layers of Eccosorb AN-72) in a metal cylinder closed on one end. The target fit neatly over the antenna aperture, with the metal "can" minimizing contributions from the surroundings. Dipped in LN, inverted until the liquid had largely ceased to drip from the Eccosorb tips, and then placed over the antenna aperture, the target proved to be stable in temperature in any orientation for periods greater than 32 seconds.

We performed additional tests to ensure that the LN target itself did not change temperature in a position-dependent fashion. Although its temperature in either orientation was stable in time over the 32-second duration of a single observation, it was possible that LN collecting in the Eccosorb tips could alter the target's antenna temperature. We tested for this effect in two ways. With the radiometer pointing up, we compared the output as the radiometer viewed the LN target with varying amounts of LN dripping from the Eccosorb. We observed no change at the 15 mK level. In addition, we compared the LN target in both the up and down positions to an independent cold target (either the reference load with LN as cryogen or the zenith sky). We observed no position-dependent effects at the 30 mK level. We concluded that the LN target antenna temperature was independent of orientation to better than 30 mK.

Table 2 shows the results of all offset tests performed at Barcroft, for both ambient and LN targets. Since all the measurements were differential, we have arbitrarily taken the effect at zenith to be the zero point of the tests. The results were generally consistent from day to day, and had noise levels consistent with control runs in which the radiometer did not move.

The only non-zero effect appeared when the radiometer was inverted. With an ambient target over the antenna, the radiometer output was 26±2 mK colder when the

radiometer pointed down. With a LN target replacing the ambient target, the effect doubled, to 52±34 mK. This result, although consistent with the ambient result, could not test Eq. 5 to precision sufficient to identify the cause. The simplest cause, a small variation in gain, should scale as the sum of the target and system temperatures and would be expected to decrease by a factor 0.6 when the antenna viewed the colder LN target. Changes in system temperature are independent of target temperature, and should remain constant as the targets are switched, while changes in internal reflection coefficients or insertion losses predict a much larger signal when the LN target is viewed. The LN test better approximated a 4 K load; consequently, we chose to use the results of the LN test, unscaled, to correct the measured signal difference between the cold load and the zenith sky. We took the uncertainty to be the statistical uncertainty of the LN results added in quadrature with the 0.03 K limit on LN target stability. The resultant correction ΔT_{Offset} in Eq. 4 was then $\Delta T_{Offset} = -0.052 \pm 0.034$ K.

b) Sidelobe Reception

The ground was the brightest source in the vicinity of the radiometer. Although its contribution was greatly reduced by the corrugated horn antenna, ground radiation entering the antenna sidelobes could still contribute a large, angle-dependent signal to the upward-pointing radiometer, systematically altering the determinations of both $T_{A,zenith}$ and $T_{A,Atm}$. We estimated the contribution of $T_{A,Ground}$ in several ways.

We obtained a lower limit on $T_{A,Ground}$ by alternately adding and removing a large piece of sheet metal to one side of the ground shield. The simplest test used the additional "chop" shield as an extension of the ground shield. If ground radiation were entering the antenna beam without diffracting, the chop shield would block some fraction of this radiation, replacing it with reflected sky radiation (Figure 4a). We recorded the output voltage and searched for signals synchronous with the chop period. A similar test searched for radiation diffracting over the flared sections. In this case, the chop shield undercut the flares, replacing ground radiation with reflected sky radiation in the vicinity of the flares (Figure 4b). Results of both tests are shown in Table 3. The local horizon rose sharply to the west, and was visible in the main antenna lobe above the ground shield for the -40° and -30° positions. A small signal was evident in the E-plane at all angles, caused by radiation diffracting over the flared sections of the ground shields. We obtained only null results from the H-plane tests. Sidelobe response should be similar on opposite sides of the

shields for the H-plane at all angles and for the E-plane at the zenith. We therefore treated the uncertainties from these positions as correlated and added them linearly, effectively doubling the error estimates for the E- and H-plane results. The total estimated uncertainty at each angle was then the quadrature sum of the (doubled) E-plane and H-plane uncertainties.

The measured far-field beam pattern convolved with a flat horizon yielded an upper limit of the ground contribution $T_{A,Ground}$, provided the contribution from areas near the radiometer was adequately described by the far-field beam pattern. Although the ground was within 1.5 m of the horn aperture, and thus within the near field of the horn alone, we measured the far-field beam pattern with the pyramidal ground shield in place over the horn. The shield terminated in flared sections with flare radius 8 cm which did not move relative to the horn. The diffraction pattern over the flared sections should have been independent of source distance provided the source was several wavelengths from the flares; hence, the response of the horn/shield combination was adequately described by the measured far-field beam pattern (*i.e.*, the ground shield acted as a reflecting surface, not a continuation of the horn antenna). We concluded that ground emission with the horn/shield combination could be modelled to better accuracy than with the horn alone. With the ground treated as an ambient blackbody, the beam response convolved with a flat horizon yielded upper limits to the ground contribution as a function of angle, as reported in Table 3.

The value of $T_{A,Ground}$ measured by chop tests was somewhat lower than the value expected from the beam pattern. With the radiometer pointed at the zenith, we measured 3^{+14}_{-3} mK ground emission instead of the expected 23±5 mK. The change in $T_{A,Ground}$ as the radiometer tipped showed similar behavior; at 30° we observed a signal of 5^{+5}_{-2} mK instead of 36±5 mK, and at 40° we observed 10^{+5}_{-2} mK instead of 47±10 mK. The two results can be reconciled if the direct sidelobe tests did not modulate the entire diffracted ground signal. We treated the direct tests as a lower limit to $T_{A,Ground}$, and the beam pattern convolution as an upper limit. We took as the estimate of $T_{A,Ground}$ the arithmetic mean of the two methods, with an uncertainty equal to half the spread between them. A substantial fraction of $T_{A,Ground}$ was a constant arising from the response at large angles (≥130°) which always viewed the ground for any of the radiometer positions used. This contribution did not change as the radiometer tipped; hence, the differential uncertainty in $T_{A,Ground}$ between the zenith and 40° was somewhat less than the absolute uncertainty at either position. We estimated the differential uncertainty as the quadrature sum of the

uncertainties in the differential signal calculated from the upper and lower limits. The estimated values for $T_{A,Ground}$, both absolute and differential, are summarized in Table 4. We used these values in Eq. 4 and in calculation of $T_{A,Atm}$.

c) Calibration Stability

An ideal total-power radiometer with system temperature T_{system}, bandwidth B, calibration coefficient G, and integration time τ viewing a target of antenna temperature T_{Target} has RMS noise described by

$$\Delta T_{noise} = (T_{system} + T_{Target}) \left\{ \frac{1}{B\tau} + \left(\frac{\delta G}{G}\right)^2 \right\}^{1/2}$$

(Kraus, 1969). If gain fluctuations $\delta G/G$ are negligible, the noise is gaussian and decreases as the inverse square root of the integration time. By taking data when the radiometer observes a stable target, averaging the data into successively longer blocks, and comparing the resultant RMS scatter to the predicted $\tau^{-1/2}$ spectrum, we can assess the effects of short-term changes in calibration. The tests showed non-gaussian fluctuations in calibration to be the dominant source of noise in the instrument. For the 234 K system temperature, 500 MHz bandwidth, and 2 second integration time of the radiometer, the predicted noise was 7 mK between adjacent data points (viewing a 4 K target). The measured value was 33 mK, which decreased approximately as $\tau^{-1/2}$ on time scales between 32 and 64 seconds. On longer time scales the noise increased slightly from its minimum value.

The effect of short-term calibration changes on the measurements of $T_{A,zenith}$ and $T_{A,Atm}$ could be assessed directly using data from observations of stable targets. We averaged the data into blocks 24 seconds in duration separated by a time Δt, and looked for changes in the RMS as the time delay Δt was increased. The 24-second integration time and time delay Δt between 32 and 112 seconds corresponded to the time scales typical of the atmospheric and zenith sky measurements. The noise increased as $\Delta t^{0.4\pm0.1}$, and was larger when viewing the warmer ambient target by a factor 1.8 ± 0.1. Both were consistent with a random-walk process in the calibration coefficient of the radiometer, with variations $\delta G/G \sim 10^{-4}$ on time scales of several minutes.

The fluctuations served to inject noise at the 20—30 mK level to the signal differences used to determine $T_{A,zenith}$ and $T_{A,Atm}$. Drifts in the calibration could also systematically alter the mean values by adding a systematic signal

$$\Delta T_{gain} = \frac{\delta G(\Delta t)}{G} T_{system}$$

to the difference between two observations spaced a time Δt apart, if the gain drifts had a preferred sign. As described below, the data analysis routine included removal of a linear drift in calibration over the course of a single scan. We analyzed the control runs of stable data as though they were atmospheric or zenith sky measurements and removed the linear component of the drift on time scales of 128 to 224 seconds. The resultant data sets had zero mean and RMS noise consistent with the 20—30 mK noise described above. We concluded that fluctuations in radiometer calibration dominated the system noise, but served only to inject additional noise at the 20—30 mK level and did not systematically alter the signal differences.

d) Calibration Linearity

The major source of non-linear behavior in the RF chain was the HP 8473B detector diode. Typically, this device exhibits non-linearities for output signals above 4—5 mV. The radiometer design deliberately kept the RF gain low to keep the diode in the linear regime for all but the ambient target. The signals for LHe and LN loads were in the linear regime of the diode (-2.0 and -2.9 mV respectively), while the ambient target (-5.3 mV) was slightly saturated.

Scans measuring $T_{A,zenith}$ and $T_{A,Atm}$ calculated the calibration coefficient G using the ambient-LHe or ambient-sky signal difference, which was slightly saturated. We corrected the calibration of the radiometer by pointing it at three targets in rapid succession: the reference target ($T_{A,load}$ = 3.6 K), the LN target ($T_{A,LN}$ = 73.8 K) and an ambient target ($T_{A,Amb}$ ~ 270 K). For some tests the zenith sky replaced the cold load as the coldest target. From the three targets, three calibration coefficients may be determined. The ratio of calibrations determined by LHe-LN to LHe-ambient targets fixed the correction to be applied to the LHe-ambient scan calibrations for saturation effects at 0.985±0.005.

e) RFI

Another unwanted contribution to the sky signal was RFI. Near major population centers, commercial and government microwave communication links raised $T_{A,zenith}$ to over 50 K. The situation was considerably better at a remote location; nevertheless, we searched for RFI at Barcroft before beginning any other tests. With a spectrum analyzer replacing the detector diode, we observed no RFI at 10 kHz resolution over the range 5.75—8.75 GHz, corresponding to a limit on RFI contributions of $T_{A,RFI} < 0.005$ K at any of the angles used.

f) Pointing

Systematic differences between the zenith angle θ used in atmospheric analysis and the true zenith angle θ' of the radiometer could alter the calculated $T_{A,Atm}$ from the true value. We measured the pointing of the radiometer repeatedly and found it to be quite stable over time scales of a single run (~ 1 hour) and the entire stay at White Mountain (Table 5). The bubble clinometer used to establish the absolute pointing has an uncertainty of $\pm 5'$ in its zero point. This uncertainty dominated the pointing uncertainty.

g) Cross-Talk

The radiometer shared the recording system with radiometers operating at 1.5, 3.8, and 90 GHz, as well as temperature information from the reference cold load. We tested for cross-talk between the instruments. While the 7.5 GHz radiometer observed a stable ambient target, we alternately covered and uncovered the antenna of one of the other radiometers with an ambient target, causing a large square-wave output signal for that radiometer. We then examined the output of the 7.5 GHz radiometer for any signals synchronous with this square-wave signal. We observed no effects at the 5 mK level.

IV. DATA COLLECTION

a) Zenith Sky

The radiometer measured $T_{A,zenith}$ by comparing the signals from the cold load, the zenith sky, and the ambient target, observed in close succession. The radiometer spent 32

seconds observing the cold load, 32 seconds observing the zenith, and 16 seconds observing the ambient target. Sixteen seconds elapsed between each position, during which time we discarded all data. A complete scan sequence took 128 seconds, with only 16 seconds separating the observations of the cold load and the zenith sky. A typical observing run over the cold load lasted 40 minutes and comprised some 15 independent measurements of $T_{A,zenith}$.

We measured $T_{A,zenith}$ with LHe in the cold load on 1988 September 16, 17, and 19, obtaining 65 independent measurements of $T_{A,zenith}$ (Table 6). As a test of the scan procedure and equipment, we measured $T_{A,zenith}$ with liquid nitrogen in the cold load on the night of 1988 September 14.

b) Atmosphere

We determined the atmospheric antenna temperature by comparing the signal from the zenith sky to the signal when the radiometer tipped to angles of 30° and 40° to either side of the zenith along the E-W direction. The ground shield remained firmly attached to the radiometer throughout the entire measurement. The radiometer viewed the following targets for 32 seconds each in sequence: the sky at each of the positions -40°, -30°, zenith, +30°, and +40°, followed by the ambient target. Sixteen seconds elapsed before and after observation of the ambient target, during which time we ignored the data. A single atmospheric scan took 224 seconds. The maximum elapsed time between measurements of the zenith and any angle θ was 32 seconds. An atmospheric run typically lasted an hour and comprised 10 to 15 complete scans.

We used an alternate scanning procedure on the night of September 19 in an effort to concentrate the observing time on the eastern (+) angles which had a much smaller correction for $T_{A,Ground}$. We calibrated only once every other scan, and observed the eastern angles exclusively, observing for 32 seconds at each position in order zenith, +30°, +40°, zenith, +30°, +40°, ambient target. Again, a period of 16 seconds elapsed before and after observations of the ambient target. We ignored data from these 16-second periods. A single scan now took either 96 seconds or 160 seconds, depending on whether a calibration was included. A typical run lasted 90 minutes and comprised 20 to 30 independent scans. We measured $T_{A,Atm}$ on the nights of 1988 September 3, 4, 5, 7, 9, 11, 14, 15, 16, 17, and 19.

c) Galaxy

We measured the differential galactic profile by comparing the signal when the radiometer pointed 15° east of zenith to the signal when the radiometer pointed 15° west of zenith. The radiometer alternately observed the +15° position for 16 seconds and the -15° position for 16 seconds. The radiometer spent 16 seconds moving from one position to the other, during which time we ignored all data. Approximately once per hour we left the radiometer in the -15° position for several minutes while we placed the ambient target over the antenna for calibration.

The ±15° zenith angles chopped between two positions at declination 36° separated by 2.4 hours in right ascension (R.A.). We measured the differential galactic profile on the nights of 1988 September 5, 6, 8, and 10. Over the course of these nights, we obtained coverage of the track from R.A. = -60° to R.A. = +112°, observed simultaneously with four radiometers at 1.5, 3.8, 7.5, and 90 GHz.

V. Data Reduction and Analysis

a) Calibration

We calculated the calibration coefficient G of the radiometer by recording the voltage difference as the radiometer viewed the ambient and cryogenic targets and correcting for non-linearity:

$$G = \beta \frac{T_{A,Amb} - T_{A,load}}{S_{Amb} - S_{load}}, \tag{6}$$

where $T_{A,Amb}$ is the antenna temperature of the ambient target and S_{Amb} and S_{load} are the output voltages viewing the ambient target and cold load, respectively. We adopted a value for the saturation correction β of 0.985± 0.005 as discussed above. For atmospheric and galactic measurements the zenith sky substituted for the cold load, with Eq. 6 solved iteratively to achieve self-consistency.

Slow temperature drifts in the RF chain caused the value of G to drift on time scales of several hours. We measured G on time scales of several minutes. All analysis used a linear interpolation between successive measurements of G to reduce the effect of slow

changes in absolute calibration. Residual scatter of successive measurements of G varied by $\delta G/G < 10^{-4}$.

b) $T_{A,zenith}$

We calculated $T_{A,zenith}$ using Eq. 2 on a scan-by-scan basis. We calibrated the radiometer once per scan using the cold load and the ambient target (Eq. 6). Subsequent analysis used a calibration coefficient G(t) interpolated between successive calibrations.

c) $T_{A,Atm}$

For a radiometer with a pencil beam viewing an optically thin, planar atmosphere, $T_{A,Atm}$ may be calculated from the signal difference between the zenith and angle θ by the relation

$$T_{A,Atm} = G \frac{S_\theta - S_{zenith}}{\sec(\theta) - \sec(0)}$$

$$= G \frac{S_\theta - S_{zenith}}{\sec(\theta) - 1}, \qquad (8)$$

where S_θ and S_{zenith} are the outputs of the radiometer viewing angle θ and the zenith, respectively. For angles near the zenith, the denominator becomes very large and has the effect of multiplying noise and small residual signals from non-atmospheric sources into large sources of error. In practice, the angles θ=30° and θ=40° provide equally-spaced denominators of 6.3 and 3.2, respectively.

In fact, the above model is somewhat simplistic. The real atmosphere is curved to follow the Earth's curvature; the beam pattern of the antenna has a non-negligible width of about 12°; the atmospheric opacity causes a slight self-absorption of the signal. It can be shown (e.g. Witebsky *et al* . 1987, De Amici *et al.* 1985) that the generalization of Eq. 8 is

$$T_{A,atm} \equiv \frac{\Delta T_{Atm}}{F_0} \{ F_1 + (\frac{\Delta T_{Atm}}{F_0 T_{kin}}) F_2 + (\frac{\Delta T_{Atm}}{F_0 T_{kin}})^2 F_3 \}, \qquad (9)$$

where ΔT is the antenna temperature of the signal difference,

$$\Delta T_{Atm} = G\,(S_\theta - S_{zenith}), \qquad (10)$$

T_{kin} is the physical temperature of the atmosphere (~240 K), and F_0, F_1, F_2, and F_3 are moments of the measured beam pattern convolved with a curved atmospheric shell, evaluated numerically using the measured far-field beam pattern with the ground shield in place. We determined $T_{A,Atm}$ from Eq. 9 on a scan-by-scan basis, after correcting ΔT_{Atm} for the differential effects of ΔT_{Offset}, $T_{A,ground}$, and $T_{A,Galaxy}$.

Although we measured $T_{A,Atm}$ at four zenith angles, we used only the two eastern angles in the analysis. The western angles had much larger corrections for sidelobe contributions from the higher horizon profile to the west. The value of $T_{A,Atm}$ for each scan is the arithmetic mean of the +30° and +40° scans.

The linear interpolation for G removed the major effects of gain drifts during the course of a single scan. Non-linear changes large enough to effect the estimate of $T_{A,Atm}$ occurred rarely. The pattern of the sky observations (western angles first followed by the zenith and the eastern angles) provided a distinctive signature for such processes. The output signal when observing a cold target was dominated by the system temperature:

$$S \sim \frac{1}{G(t)}[T_{system} + T_\theta] \sim \frac{1}{G(t)} T_{system}$$

Residual drifts in G(t) on time scales of a single scan typically added a signal ΔS to the west-zenith signal difference, and a signal $-\Delta S$ of the opposite sign to the east-zenith signal difference, which occurred in the opposite time order. The calculated values for $T_{A,Atm}$ should be displaced by roughly equal amounts above and below the mean value. We observed this signature in 10 of the 285 total scans. The suspect scans were discarded.

d) $T_{A,Galaxy}$

We obtained a differential profile of the galaxy by combining data from the nights of 1988 September 5, 6, 8, and 12. We binned the data into 4° wide bins, which allowed each binned sky position to be observed for 15 independent scans per night. Over the course of the four nights, each bin accumulated between 20 and 50 independent observations of the differential galactic signal. The differential local horizon can conceivably add a constant signal difference to the sky difference. We did not obtain the

complete sky coverage needed to enforce closure on the data. Instead, we calculated the mean of all difference pairs, and arbitrarily removed the resultant value of 12.4 mK from the data set.

VI. RESULTS

a) $T_{A,zenith}$

The radiometer made 65 independent measurements of $T_{A,zenith}$. The results are presented in Table 6, without corrections for systematic effects. The data from various nights were in good agreement, showing no more variation than would be expected from daily atmospheric changes.

b) $T_{A,Galaxy}$

The measured differential galactic signal between R.A. of -60° and +112° is shown in Figure 5, along with the results of a simple galactic model. The double-lobed chopped-beam signature towards the galactic plane is clearly visible. The galactic model uses an extrapolation of 408 MHz maps from Haslam *et al.* (1982), scaled by a position-independent spectral index of -2.75, and a compilation of thermal sources at 2.7 GHz, with spectral index -2.1. The signal was above the noise level only in the galactic plane, which was dominated by thermal emission; in this region, we observed 0.89±0.06 of the expected (HII + synchrotron) signal. Lacking better sensitivity in regions off the galactic plane where synchrotron emission is dominant, we were unable to distinguish between the thermal and synchrotron components within the plane.

The differential galactic scans confirmed that our simple model was not in serious error, as the measured galactic signal lay within 10 mK of the predicted signal (Figure 5). We used this simple model to subtract the differential galactic signal from the atmospheric and zenith sky scans. The maximum error entailed is 0.05 K in $T_{A,Atm}$ and 0.01 K in $T_{A,zenith}$ if the galactic plane crossed the zenith during observations. Uncertainties in the galactic signal off the plane of the galaxy (*i.e.*, during most of our atmosphere scans and all of the CMB scans) were much smaller (0.005 K).

c) $T_{A,Atm}$

The radiometer performed numerous atmospheric scans at Barcroft. The values for $T_{A,Atm}$ at each of the four scan angles are presented in Table 7 for all nights in which we measured $T_{A,zenith}$. The angles to the west had a large correction for $T_{A,Ground}$; the mean value for $T_{A,Atm}$ included data from the eastern (+) angles exclusively. Atmospheric temperatures at the eastern angles were in excellent agreement with each other. $T_{A,Atm}$ measured at +40° was 20±12 mK warmer than the value measured at 30°. There was no statistical evidence for unidentified systematic offsets in the mean atmospheric data.

The data at 30° had a mean RMS scatter of 221 mK, while the RMS at 40° was 162 mK. This noise was consistent with the small fluctuations in the calibration constant discussed in §IV, multiplied by the $[\text{secant}(\theta) - 1]^{-1}$ angular dependence of the atmospheric signal differences, and approximated a gaussian distribution within each hour-long observing run.

The error budget for each atmospheric angle is given in Table 8. Systematic corrections are presented as an additive correction to $T_{A,Atm}$. The dominant terms are the differential contributions of $T_{A,Ground}$ and ΔT_{Offset} between the zenith and scan angle θ. All the terms in Table 8 have been measured; the associated uncertainties represent the 68% confidence level of the measurement.

d) $T_{A,CMB}$

We determined $T_{A,CMB}$ by solving Eq. 4 on a scan-by-scan basis. Each of the terms in Eq. 4 has been measured, some in more than one fashion. The estimated error budget for the CMB measurement is given in Table 9. The systematic uncertainty of 0.069 K was dominated by the uncertainty in the largest foreground signal, the atmosphere. We did not measure $T_{A,Atm}$ concurrently with $T_{A,zenith}$; instead, we used the values for $T_{A,Atm}$ from each night fitted to a linear drift. As we did not observe the atmosphere to vary dramatically throughout any night, the uncertainty in $T_{A,CMB}$ incurred in the atmospheric interpolation was small. The resultant values for $T_{A,CMB}$ are given in Table 10, both for each of the four observing runs, and as a complete data set.

The individual values for $T_{A,CMB}$ had a gaussian distribution (Figure 6). The RMS width of the distribution was 0.050 K with 65 data points; consequently, we adopted 0.006 K as the estimate of the statistical uncertainty in the mean value of $T_{A,CMB}$. Adding

the statistical uncertainty in quadrature with the 0.072 K systematic uncertainty, we obtained a value for the antenna temperature of the CMB of

$$T_{A,CMB} = 2.413 \pm 0.072 \text{ K (68\% C.L.)}$$

Using Eq. 1 to convert this value to thermodynamic temperature yielded the final result of

$$T_{CMB} = 2.59 \pm 0.07 \text{ K}$$

VII. DISCUSSION

a) $T_{A,Atm}$

The atmosphere at low frequencies is not completely understood. The dominant component of atmospheric emission below 10 GHz is continuum O_2 emission, with a minor, variable contribution from water vapor. Models of atmospheric emission with water vapor content typical of our high-altitude site (2—5 mm H_2O) predict $T_{A,Atm}$ at 7.5 GHz in the range 0.89—0.96 K (Liebe 1988, 1985, 1981). The mean $T_{A,Atm}$ at 7.5 GHz measured during LHe observations was 1.08±0.06 K. From day to day, we observed RMS scatter of ~0.07 K. Both the magnitude and variability of this signal were slightly larger than predicted.

An increase in signal magnitude and variability compared to modelled atmospheric emission is a feature common to several recent low-frequency measurements of the atmosphere (*e.g.* Kogut *et al.* 1988, De Amici *et al.* 1988). In general, the model parameters are fitted to the line features of the emission peaks, and may be much poorer descriptions of the windows of astrophysical interest. Several rather *ad hoc* corrections to the contribution from the O_2 continuum and the 22 GHz water line have been proposed (*e.g.*, Danese and Partridge 1989 and references therein), which tend to increase the signal magnitude and variability below 10 GHz. The resultant variability in $T_{A,Atm}$ at 7.5 GHz is in better (but still poor) agreement with the observed signal variability.

The value of $T_{A,Atm}$ at 7.5 can be compared to measurements from White Mountain at nearby frequencies. Results from 3.8, 7.5, and 10.0 GHz are summarized in Table 11. The model of atmospheric emission predicts $T_{A,Atm}$ at 7.5 GHz to be smaller than at 10

GHz by 100—150 mK, and larger than 3.8 GHz by 80—130 mK. The observed differences were 100 and 125 mK, respectively, in agreement with the model differences if not the magnitudes. There is no evidence for undetected systematics in the atmospheric measurements at 7.5 GHz. One is led to the conclusion that, at frequencies below 10 GHz, the data are better understood than the atmospheric model.

b) T_{CMB}

Table 12 lists recent precise CMB measurements, shown in Figure 7. The measurement at 7.5 GHz is in excellent agreement with other ground-based results, which in turn are in poor agreement with measurements at higher frequencies using other techniques. The mean of all recent ground-based measurements, weighted by their uncertainties, is 2.647±0.031 K (χ^2 = 6.9 for 8 DOF), compared to the weighted mean of 2.786±0.013 K (χ^2 = 7.7/6 DOF) for all other measurements below 0.1 cm. The weighted average is a valid estimate of the mean of the parent distribution, provided the uncertainties are uncorrelated and no spectral features are present. In fact, the ground-based measurements share to some extent a number of systematic uncertainties, most notably in the measurement of the atmosphere and the cold load. The CN results, too, share some fraction of the systematic uncertainty. The weighted uncertainties are thus underestimated to some extent; however, this does not alter the fact that ground-based measurements report results that are systematically lower than other techniques. One is led to the conclusion that either set of measurements has undetected systematics, or that additional spectral features may exist in the Rayleigh-Jeans portion of the CMB spectrum.

c) Consequences for Spectral Distortions

The Rayleigh-Jeans portion of the CMB spectrum can distinguish among some competing models explaining the apparent distortion at sub-mm wavelengths. Emission from warm dust at late epochs ($z \sim 30$) will leave the Rayleigh-Jeans spectrum undistorted, while models invoking Compton scattering from a hot medium predict the Rayleigh-Jeans temperature to be reduced by an amount $\delta T_{RJ} = T_R(1 - 2y)$, where T_{RJ} is the CMB temperature in the Rayleigh-Jeans region, T_R is the undistorted CMB temperature, and y is the Compton parameter

$$y(z) = -\int_0^z \frac{k[T_e(z) - T_R(z)]}{m_e c^2} \sigma_T \, n_e(z) \, c \frac{dt}{dz'} dz',$$

where m_e, $T_e(z)$ and $n_e(z)$ are the electron mass, temperature, and density at redshift z, and σ_T is the Thomson cross section (Zel'dovich and Sunyaev 1969, Danese and De Zotti 1978). The best fit to a Comptonized spectrum yields values $T_R = 2.818 \pm 0.019$ K and $y = 0.020 \pm 0.010$ with $\chi^2 = 34.4$ for 16 DOF (95% confidence level uncertainties). The significance of the values for T_R and y result entirely from the measurements in the Wien spectrum; if only points with $\lambda \geq 0.1$ cm are considered, the values drop to $T_R = 2.789 \pm 0.022$ K and $y = 0.009 \pm 0.010$ with $\chi^2 = 22.1$ for 14 DOF.

A large fraction of the χ^2 in various models fitting the CMB spectrum is attributable to the discrepancy between ground-based and other techniques in the Rayleigh-Jeans portion of the spectrum. For all data to be consistent within their error bars would require a drop in CMB brightness below ~ 1 cm, characteristic, for example, of Compton μ-distortions (Danese and De Zotti 1980, Sunyaev and Zel'dovich 1970). The required energy release, $\delta E/E = 0.004$, is consistent with previously established upper limits (Smoot *et al.* 1988). However, the low-frequency CMB spectrum has been observed solely by ground-based measurements and has not been tested by a method with different systematics. In a field with a history of unsuspected systematic effects, confirmation of any suspected spectral feature should be obtained by as many methods as possible. A balloon-borne spectral measurement between 1 and 10 GHz would be of great interest in resolving the question of possible CMB distortions below 1 cm.

VIII. CONCLUSIONS

We have measured the brightness temperature of the CMB at frequency 7.5 GHz to be 2.59 ± 0.07 K. The largest contribution to the uncertainty of the measurement is the contribution of diffracted ground radiation entering the antenna sidelobes during tip scans to measure the antenna temperature of the atmosphere. Ground-based CMB measurements yield results systematically lower than measurements at higher frequencies using other techniques. The apparent conflict can be resolved by postulating undetected systematics in either set of measurements, or a possible CMB distortion at wavelengths below 1 cm.

ACKNOWLEDGEMENTS

This experiment could never have occurred without the skilled help of many people. We wish to thank Jon Aymon, John Gibson, Jenny Hwang, Jay Levin, Larry Levin, Faye Mitschang, Luis Tenorio, and the staff and crew of the White Mountain Research Station for their assistance. This work was supported by NSF grant DPP-8716548 and by the Department of Energy under contract DE-AC03-76SF000098.

APPENDIX A: ANTENNA TEMPERATURE OF THE REFERENCE TARGET

The reference target/radiometer combination may be modelled without loss of generality as a perfect radiometer observing a perfect absorber, with a series of reflecting and absorbing surfaces between them. The antenna temperature of the load is then the sum of the power emitted by the load (attenuated by the surfaces between the load and the radiometer) and the power broadcast by the radiometer and reflected back by the load (in practice, the attenuation is negligible). We will consider these two terms independently.

a) Reflection

The reflection coefficient of the cold load is the coherent sum of the individual amplitude reflection coefficients. Radiation reflecting from surfaces within a coherence length L of the radiometer can interfere coherently with the broadcast radiation. We include this effect as an effective phase term for each reflecting surface, where the phase of reflections internal to the radiometer has been selected as the reference phase. The amplitude reflection coefficient r of the cold load is thus

$$r = r_R + r_{F1}e^{i\phi F1} + r_{F2}e^{i\phi F2} + r_He^{i\phi H} + r_Ae^{i\phi A} + r_{P1}e^{i\phi P1} + r_{P2}e^{i\phi P2} + r_Te^{i\phi T},$$

where subscripts R, F, H, A, P, and T refer to the radiometer, Fluorglas windows, helium liquid/gas interface, microwave absorber, polyethylene windows, and transition from horn to radiometric cavity, respectively. The magnitudes of the last three terms are small, and may be neglected with negligible error:

$$r \approx r_R + r_{F1}e^{i\phi F1} + r_{F2}e^{i\phi F2} + r_He^{i\phi H} + r_Ae^{i\phi A}. \qquad (A1)$$

The reflected signal is proportional to the square of the reflection coefficient and the difference in broadcast temperature between the radiometer and the cold load,

$$\Delta T_{ref} \approx |r|^2 (T_{Broad} - T_{Abs})$$

where the temperature of the load to lowest order is simply the temperature of the absorber. Squaring Eq. A1 gives the sum

$$|r|^2 = |r_R|^2 + |r_{F1}|^2 + |r_{F2}|^2 + |r_H|^2 + |r_A|^2$$

$$+ 2r_R r_{F1} \cos(\phi_{F1})$$
$$+ 2r_R r_{F2} \cos(\phi_{F2})$$
$$+ 2r_R r_H \cos(\phi_H)$$
$$+ 2r_R r_A \cos(\phi_A)$$

$$+ 2r_{F1} r_{F2} \cos(\phi_{F1} - \phi_{F2})$$
$$+ 2r_{F1} r_H \cos(\phi_{F1} - \phi_H)$$
$$+ 2r_{F1} r_A \cos(\phi_{F1} - \phi_A)$$
$$+ 2r_{F2} r_H \cos(\phi_{F2} - \phi_H)$$
$$+ 2r_{F2} r_A \cos(\phi_{F2} - \phi_A)$$
$$+ 2r_H r_A \cos(\phi_H - \phi_A). \qquad \text{(A2)}$$

Equation A2 is valid for radiation coherent over regions much larger than the separations between any two surfaces. In practice, the 500-MHz bandwidth B of the radiometer implies a coherence length $\Lambda = c/B = 60$ cm, comparable to the separations involved. Over distances $x \sim \Lambda$, the phase coherence diminishes by an amount $\zeta(z)$, where

$$\zeta(z) = \left[\frac{\sin(z)}{z}\right]^2,$$

where the phase difference z is related to the separation x between two surfaces by

$$z = \frac{2\pi x}{\Lambda}.$$

Each cosine term in Eq. A2 must be multiplied by the function $\zeta(z)$ applicable for the separation between the reflecting surfaces.

In addition, there is an effect from illumination. The horn antenna occupies ~6% of the aperture of the load; in addition, the radiometer beam diverges as the distance from the horn mouth increases. Only a fraction Γ of the power broadcast from the radiometer and reflecting from a surface actually re-enters the antenna; the rest reflects from the top plate and is absorbed by the microwave absorber. Each term in Eq. A2 must also be multiplied by the illumination Γ of the reflecting surface. With these corrections, the reflection coefficient of the reference load may be written as

$$|r|^2 = |r_R|^2$$

$$+ |r_{F1}|^2 \Gamma_{F1} + |r_{F2}|^2 \Gamma_{F2} + |r_H|^2 \Gamma_H + |r_A|^2 \Gamma_A$$

$$+ 2r_R r_{F1} \cos(\phi_{F1}) \Gamma_{F1} \zeta(z_{F1})$$
$$+ 2r_R r_{F2} \cos(\phi_{F2}) \Gamma_{F2} \zeta(z_{F2})$$
$$+ 2r_R r_H \cos(\phi_H) \Gamma_H \zeta(z_H)$$
$$+ 2r_R r_A \cos(\phi_A) \Gamma_A \zeta(z_A)$$

$$+ 2r_{F1} r_{F2} \cos(\phi_{F1} - \phi_{F2}) \Gamma_{F1} \zeta(z_{F1,F2})$$
$$+ 2r_{F1} r_H \cos(\phi_{F1} - \phi_H) \Gamma_{F1} \zeta(z_{F1,H})$$
$$+ 2r_{F1} r_A \cos(\phi_{F1} - \phi_A) \Gamma_{F1} \zeta(z_{F1,H})$$
$$+ 2r_{F2} r_H \cos(\phi_{F2} - \phi_H) \Gamma_{F2} \zeta(z_{F2,H})$$
$$+ 2r_{F2} r_A \cos(\phi_{F2} - \phi_A) \Gamma_{F2} \zeta(z_{F2,H})$$
$$+ 2r_H r_A \cos(\phi_H - \phi_A) \Gamma_H \zeta(z_{H,A}) \qquad \text{(A3)}$$

All terms contributing to Eq. A3 are listed in Table A1. Equation A3 consists of a constant term (proportional to the summed power reflectivity of each surface and the illuminations), a term dependent on the product of the amplitude coefficients of the radiometer and reflecting surfaces (modulated by the phase ϕ between the radiometer and the reference load), and a term dependent on the amplitude reflection coefficients within the load (modulated by their separation). The power reflection internal to the radiometer, $|r_R|^2$, may be neglected as it cancels in the sky—load comparison (provided $T_{A,zenith}$ is not greatly different from $T_{A,Load}$).

The phase-independent terms sum to $\Sigma|r_i|^2 \Gamma_i = 2.0 \times 10^{-5}$. Multiplied by the 298 K temperature difference between the radiometer's broadcast temperature and the absorber temperature, these terms contribute 6±3 mK to $T_{A,Load}$.

Terms dependent on the single phase ϕi between the radiometer and the i^{th} reflecting surface can be calculated knowing the positions of each surface. The terms are small: were all of the terms to add coherently, the reflection dependent on radiometer position would sum to < 1 mK. As a precaution, we tested for this effect by sliding the radiometer on a specially-constructed extension of the radiometric wall. We observed no signal while changing the phases ϕ_i by more than 4π. Terms dependent on the radiometer's position contribute 0±1 mK to $T_{A,Load}$.

Of the remaining terms, only the first has an appreciable magnitude. The term

$$2r_{F1}r_{F2}\cos(\phi_{F1} - \phi_{F2})\,\Gamma_{F1}\,\zeta(z_{F1,F2})\,.$$

represents coherent reflection between the two Fluorglas IR-blocking windows. The windows are spaced 5 cm apart; consequently, the phase term between them has a nominal value -1. In practice, we cannot be sure that gas pressure does not force the windows closer together. We take this term to be 0±4 mK instead of the nominal -4 mK. Including the 3 mK power reflection from the polyethylene windows (neglected after Eq. A1) gives the total estimated reflected power of 6±5 mK.

b) Emission

Emission properties of the reference load are summarized in Table A1. The temperatures for the Fluorglas windows are taken from sensors on the radiometric wall where the windows attach. The IR heat load may heat the windows to a somewhat higher temperature.

The 78-cm diameter radiometric wall is a good approximation to free-space. We estimate emission from the false wall by convolving the far-field beam pattern with the radiometric wall, using the emissivity of a thin aluminum layer. The aluminum foil contributes <1 mK to $T_{A,Load}$. In addition, there are two joints in the radiometric wall at the locations of the Fluorglas windows. Modelling emission from the joints as blackbody gives an upper limit to their contribution of 6 mK. We estimated the total contribution to $T_{A,load}$ from emission of warm parts of the load as 13 ± 7 mK.

The microwave absorber has an emissivity > 0.999. Its thermodynamic temperature is that of the liquid helium bath. At the ambient pressure of 481 mm Hg, helium boils at 3.771 ± 0.002 K. Converting to antenna temperature at 7.5 GHz and adding the minor reflection and emission terms gives the final value for the reference temperature:

$$T_{A,Load} = 3.613 \pm 0.009 \text{ K}$$

TABLE 1

PROPERTIES OF THE RADIOMETER

Parameter	Value
Passband	7.25—7.75 GHz
System Temperature	234 ± 3 K
Sensitivity	0.011 K $Hz^{-1/2}$ (Predicted)
	0.044 K $Hz^{-1/2}$ (Measured)
Calibration	49.2 K/V
Beam FWHM	20° ± 2°

TABLE 2

POSITION-DEPENDENT EFFECTS

	Δ(180)[a]	Δ(-40)	Δ(-30)	Δ(+30)	Δ(+40)
Ambient	-26±2	20±7	2±2	-1±3	2±4
LN	-52±17	---	---	---	---
ΔT_{Offset}	-52 ± 34	20±7	2±2	-1±3	2±4

[a] $\Delta(\theta)$ is the difference $G(S_{zenith} - S_\theta)$, in mK. A positive result means the zenith appears warmer than angle θ. 180° is the down position looking into the cold load.

TABLE 3

UPPER AND LOWER LIMITS TO SIDELOBE RECEPTION[a]

Test	-40° (mK)	-30° (mK)	zenith (mK)	+30° (mK)	+40° (mK)
E-plane extension	84±12	24±4	-11±4	---	---
E-plane diffraction	12±5	-12±9	3±3	5±2	10±2
H-plane diffraction	---	-3±2	-1±3	-5±3	-5±3
Total Direct	96 ± 15	24^{+14}_{-4}	3^{+8}_{-3}	5^{+5}_{-2}	10^{+5}_{-2}
Beam Pattern	---	---	23 ± 5	36 ± 5	47 ± 10

[a] The difference between the signal without the extra shield and the signal with the extra shield in place is shown for each of the atmospheric scan angles. Ground radiation blocked by the extra shield has a positive sign. E- and H-plane refer to the sides of the ground shield corresponding to the E- and H-planes of the horn.

TABLE 4

ESTIMATED $T_{A,GROUND}$

	-40° [a] (mK)	-30° (mK)	zenith (mK)	+30° (mK)	+40° (mK)
$T_{A,Ground}$	125±23	45±18	13±10	21±15	29±18
$\Delta T_{A,Ground}$ (θ - zenith)	112±19	32±16	---	8±8	16±13

[a] The higher horizon to the west rises above the ground shield. $T_{A,Ground}$ for -40° and -30° is given by the value for the corresponding eastern angle plus the "Total Direct" contribution from Table 3.

TABLE 5

MEASURED POINTING

Nominal Angle	-40°	-30°	-15°	Zenith	+15°	+30°	+40°
Mean Angle	-40° 19'	-30° 22'	-15° 29'	-0° 42'	+14° 31'	+29° 43'	+40° 4'
Single-run RMS	1'	1'	2'	2'	1'	2'	2'
Total 1988 RMS	8'	8'	3'	2'	2'	2'	6'

TABLE 6

MEASURED $T_{A,ZENITH}$[a]

Date (1989)	Time (UT)	Number of Scans	Calibration (K/V)	$G(S_{zenith} - S_{load})$ (mK)	$T_{A,load}$ (mK)	$T_{A,zenith}$ (mK)
Sept 16	5:45—6:15	16	48.978±0.003	-107±10	3613	3506±10
Sept 16	8:28—9:13	21	48.585±0.007	-147±11	3613	3466±11
Sept 17	11:45—12:07	11	48.166±0.013	-123±13	3613	3490±12
Sept 19	10:13—10:47	17	48.234±0.013	-163±12	3613	3450±12

[a] Quoted uncertainties are statistical only and assume a gaussian distribution. No corrections have been made for $T_{A,Atm}$, $T_{A,Gal}$, $T_{A,Ground}$, or ΔT_{Offset}.

TABLE 7

MEASURED $T_{A,ATM}$[a]

Date (1989)	Time (UT)	-40° (mK)	-30° (mK)	+30° (mK)	+40° (mK)	Mean $T_{A,Atm}$ (mK)
Sept 16	3:15—4:18	1301±44	1134±57	1078±48	1113±55	1100±49
	5:03—5:28	1113±37	900±62	1166±50	1158±32	1162±39
	6:29—7:05	1123±53	879±75	1055±79	1133±49	1094±62
	7:42—8:15	1215±58	983±105	1201±49	1177±34	1189±31
	9:24—10:01	1139±53	1008±44	1160±67	1113±43	1137±49
	11:46—12:12	1213±38	894±48	1035±58	1091±37	1064±45
Sept 17	8:26—9:03	1127±43	838±64	1245±63	1243±40	1244±48
	10:18—11:02	1098±41	869±84	1081±58	1160±26	1121±39
	12:38—13:08	1129±56	808±80	913±86	990±35	952±57
Sept 19	9:07—10:03	---	---	1046±42	1095±24	1071±31
	11:02—11:48	---	---	1088±43	1080±34	1084±33

[a] Quoted uncertainties are statistical only and assume a gaussian distribution. Systematic uncertainties are indicated in Table 8.

TABLE 8

CONTRIBUTIONS TO ATMOSPHERIC ERROR BUDGET[a]

Effect	Uncertainty	Correction to $T_{A,Atm}$ (mK)			
		-40°	-30°	+30°	+40°
$T_{A,Ground}$	13 mK	-359±61	-201±101	-52±52	-52±42
ΔT_{Offset}	5 mK	+64±22	+12±12	-6±20	+6±13
$T_{A,Galaxy}$	3 mK	0±10	0±18	0±18	0±10
Beam Pattern	20±2° FWHM	0±14	0±14	0±14	0±14
Pointing	±5'	0±7	0±7	0±7	0±7
Absolute Gain	±0.4%	0±4	0±4	0±4	0±4
Total Systematics		-295±68	-189±105	-58±61	-46±48
Statistical Uncertainty		47	69	59	37
Total Uncertainty		83	126	85	61

[a] Systematic corrections have been multiplied by the $[\sec(\theta)-1]^{-1}$ factor; the uncertainties have been added in quadrature. The statistical uncertainty for each angle is the mean value from all scans Sept 16—19.

TABLE 9

CONTRIBUTIONS TO CMB ERROR BUDGET[a]

Effect	Magnitude	Uncertainty (mK)
$T_{A,Atm}$	1083 mK	55
ΔT_{Offset}	52 mK	34
$T_{A,Ground}$	3 mK	20
$T_{A,Load}$	3629 mK	9
$T_{A,Galaxy}$	10 mK	5
$T_{A,RFI}$	0 mK	5
Calibration	48.5 K/V	<1
Total Systematics	---	69
Statistical Uncertainty	---	6
Total Uncertainty		69

[a] All uncertainties are 68% confidence level estimates.

TABLE 10

MEASURED VALUES FOR $T_{A,CMB}$[a]

Date	Time (UT)	Number of Scans	$T_{A,Atm}$ (K)	$T_{A,CMB}$ (K)
Sept 16	5:45—6:15	16	1.097±0.025	2.426 ± 0.010
Sept 16	8:28—9:13	21	1.085±0.025	2.404 ± 0.011
Sept 17	11:45—12:07	11	1.071±0.025	2.442 ± 0.014
Sept 19	10:13—10:47	17	1.078±0.025	2.394 ± 0.012
All Scans		65	1.083±0.012	2.413 ± 0.006

[a] The quoted uncertainties are statistical only to allow comparison of data between days. Systematic uncertainties are listed in Tables 8 and 9 for $T_{A,Atm}$ and $T_{A,CMB}$.

TABLE 11

COMPARISON OF $T_{A,ATM}$[a]

Year	3.8 GHz	7.5 GHz	10 GHz
1986	870±108	---	1200±65
1987	898±74	---	1160±83
1988	955±55	1080±55	---
Model	810—830	890—960	990—1120

[a] The quoted uncertainties are 68% confidence level and include systematic effects. Model predictions assume a range of precipitable water vapor between 2—5 mm.

TABLE 12

RECENT CMB MEASUREMENTS

Reference	Wavelength (cm)	Frequency (GHz)	TCMB (K)	Technique[a]
Sironi *et al.* 1987	50.0	0.6	2.98 ± 0.55	GB
Levin *et al.* 1988	21.3	1.41	2.11 ± 0.38	GB
Sironi and Bonelli 1986	12.0	2.5	2.79 ± 0.15	GB
De Amici (Smoot *et al.* 1989)	7.9	3.8	2.63 ± 0.11	GB
Mandolesi *et al.* 1986	6.3	4.75	2.70 ± 0.07	GB
Kogut *et al.* 1989[b]	4.0	7.5	2.59 ± 0.07	GB
Kogut (Smoot *et al.* 1989)	3.0	10.0	2.62 ± 0.06	GB
Johnson and Wilkinson 1986	1.2	24.8	2.783 ± 0.025	BB
De Amici *et al.* 1985	0.909	33.0	2.81 ± 0.12	GB
Bersanelli *et al.* 1989	0.333	90.0	2.60 ± 0.09	GB
Meyer and Jura 1985	0.264	113.6	2.70 ± 0.04	CN
	0.132	227.3	2.76 ± 0.20	CN
Crane *et al.* 1988	0.264	113.6	$2.796\ ^{+0.019}_{-0.041}$	CN
	0.132	227.3	2.85 ± 0.10	CN
Meyer *et al.* 1989	0.132	227.3	2.83 ± 0.07	CN
Matsumoto *et al.* 1988	0.116	259	2.799 ± 0.018	R
	0.0709	423	2.955 ± 0.017	R
	0.0481	624	3.175 ± 0.027	R

[a] "GB" indicates a ground-based measurement, "BB" a balloon-borne measurement, "CN" a spectroscopic measurement using the CN molecule, and "R" a rocket-borne experiment.

[b] This work.

TABLE A1

REFLECTION PROPERTIES

	Position[a] (cm)	r	Γ	ζ(z)
Radiometer (R)	0.0	0.1	1.0	---
Top IR Window (F1)	111	6.5×10^{-3}	7.9×10^{-2}	7×10^{-3}
Bottom IR Window (F2)	116	1.3×10^{-2}	7.9×10^{-2}	7×10^{-3}
LHe interface (H)	156	1.2×10^{-2}	2.1×10^{-2}	4×10^{-3}
Absorber (A)	162	3.2×10^{-3}	2.1×10^{-2}	4×10^{-3}
F1-F2	---	---	---	0.9
F1-H	---	---	---	5×10^{-2}
F1-A	---	---	---	4×10^{-2}
F2-H	---	---	---	6×10^{-2}
F2-A	---	---	---	4×10^{-2}
H-A	---	---	---	0.9

[a] The position is relative to the throat of the horn, taken as the reference for position and phase.

TABLE A1

EMISSION PROPERTIES

Material	Emissivity	Temperature (K)	Emission (mK)
Polyethylene	2.4×10^{-6}	270	0.7
Top IR Window	4.9×10^{-5}	50	2.5
Bottom IR Window	9.9×10^{-5}	30	3.0
Radiometric Wall	$\sim 10^{-4}$	4—270	< 1
Joints	1.0	30, 50	6
Total			13 ± 7 mK

REFERENCES

Adams, F.C., Freese, K., Levin, J., and McDowell, J.C. 1989, *Ap. J.* (submitted).

Bersanelli, M., Witebsky, C., Bensadoun, M., De Amici, G., Kogut, A., Levin, S., and Smoot, G. 1989, *Ap. J.*, in press.

Crane P., Heygi, D.J., Mandolesi, N., and Danks, A. 1986, *Ap. J.*, **309**, 822.

—, *et al.* 1988, *Proc. Third ESO/CERN Symposium*, in press.

Danese, L., and De Zotti, G. 1978, *Astron. Astroph.*, **68**, 157.

—, and De Zotti, G. 1980, *Astron. Astroph.*, **84**, 364.

—, and De Zotti, G. 1982, *Astron. Astroph.*, **107**, 39.

—, and Partridge, R.B. 1989, *Ap. J.* (in press).

De Amici, G., Smoot., G., Friedman, S.D., and Witebsky, C. 1985, *Ap. J.*, **298**, 710.

De Amici, G., Smoot, G., Aymon, J., Bersanelli, M., Kogut, A., Levin, S., and Witebsky, C. 1988, *Ap. J.*, **329**, 556.

Donnelly, R. J. 1967, *Experimental Superfluidity,* University of Chicago Press, Chicago Il.

Haslam, C.G.T., Salter, C.J., Stoffel, H., and Wilson, W.E. 1982, *Astr. Astroph. Suppl. Ser.*, **47**, 1.

Hayakawa, S., Matsumoto, T., Matsuo, H., Murakami, H., Sato, S., Lange, A., and Richards, P.L. 1988, *Publ. Astron.Soc Japan*, **39**, 941.

Johnson, D. G., and Wilkinson, D. T. 1986, *Ap. J. (Letters)*, **313**, L1.

Kogut, A., Bersanelli, M., De Amici, G., Friedman, S.D., Griffith, M., Grossan, B., Levin, S., Smoot, G.F., and Witebsky, C. 1988, *Ap. J.* **235**, 1.

Kraus, J. D. 1966, *Radio Astronomy*, 241-244, McGraw-Hill, New York.

Levin, S.M., Witebsky, C., Bensadoun, M., Bersanelli, M., De Amici, G., Kogut, A., and Smoot, G.F. 1988, *Ap. J.*, **334**, 14.

Liebe, H.J. 1981, *Radio Sci.* **16(6)**, 1183.

—, 1985, *Radio Sci.* **20**, 1069.

—, Manabe, T, and Hufford, G.A. 1988, *IEEE Trans.*(submitted).

Mandolesi, N., Calzolari, P., Cortiglioni, S., Morigi, G. 1986, *Ap. J.*, **310**, 561.

Matsumoto, T., Hayakawa, S., Matsuo, H., Murakami, H., Sato, S., Lange, A.E., and Richards, P.L. 1988, *Ap. J.*, **329**, 567.

Meyer, D.M., and Jura, M. 1985, *Ap. J.*, **297**, 119.

—, Roth, K.C., and Hawkins, I 1989, *Ap. J. (Lett* ers), (in press).

Sironi, G., and Bonelli, G. 1986, *Ap. J.*, **311**, 418.

—, *et al.* 1987, *Proc 13th Texas Symposium on Relativistic Astrophysics*, ed. M.P. Ulmer (Singapore:World Scientific).

Smoot, G., *et al.* 1985, *Ap. J. Lett.*, **291**, L23.

—, Bensadoun, M., Bersanelli, M., De Amici, G., Kogut, A., Levin, S., and Witebsky, C. 1987, *Ap. J. Lett.*, **317**, L45-L49.

—, Levin, M., Witebsky, C., De AMici, G., and Repaeli, Y 1988, *Ap. J.*, **331**, 653.

—, Bensadoun, M., Bersanelli, M., De Amici, G., Kogut, A., Levin, S., and Witebsky, C. 1989, *Ap. J. Lett.*, in preparation.

Sunyaev, R. A., and Zel'dovich, Ya. B. 1970, *Astrophys. Space Sci.*, **7**, 20.

Witebsky, C., Smoot, G., De Amici, G., and Friedman, S.D. 1986, *Ap. J.*, **310**, 145.

Zel'dovich, Ya. B., and Sunyaev, R.A. 1969, *Ap. Space Sci.*,**4**,301.

FIGURE CAPTIONS

Figure 1. Schematic of the RF chain.

Figure 2. Schematic of the cryogenic reference target.

Figure 3. Far-field beam pattern of the antenna, measured with (closed circles) and without (open circles) the ground shield.

Figure 4. Schematic representation of the tests used to set lower limits on $T_{A,Ground}$. The aluminum chop shield was alternately placed to block a radiation path, then removed.

Figure 5. Observed differential galactic profile (points) and the signal predicted from extrapolation of maps at lower frequencies (solid line).

Figure 6. Histogram of 65 independent measurements of $T_{A,CMB}$.

Figure 7. Recent precise CMB measurements.

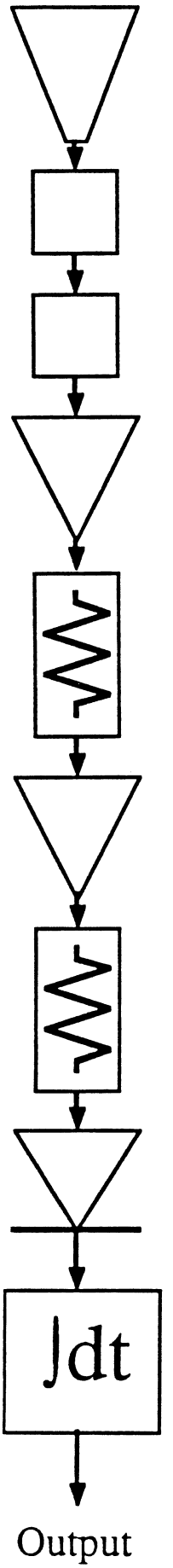

Antenna

Waveguide/Coax
Transition

Isolator

Miteq AMF-4S-7278-15
40 dB Amplifier

6 dB Attenuator

Avantek SA82-2706
25 dB Amplifier

13 dB Attenuator

HP 8473B
Detector Diode

x2500 DC Amplifier
Ideal Integrator

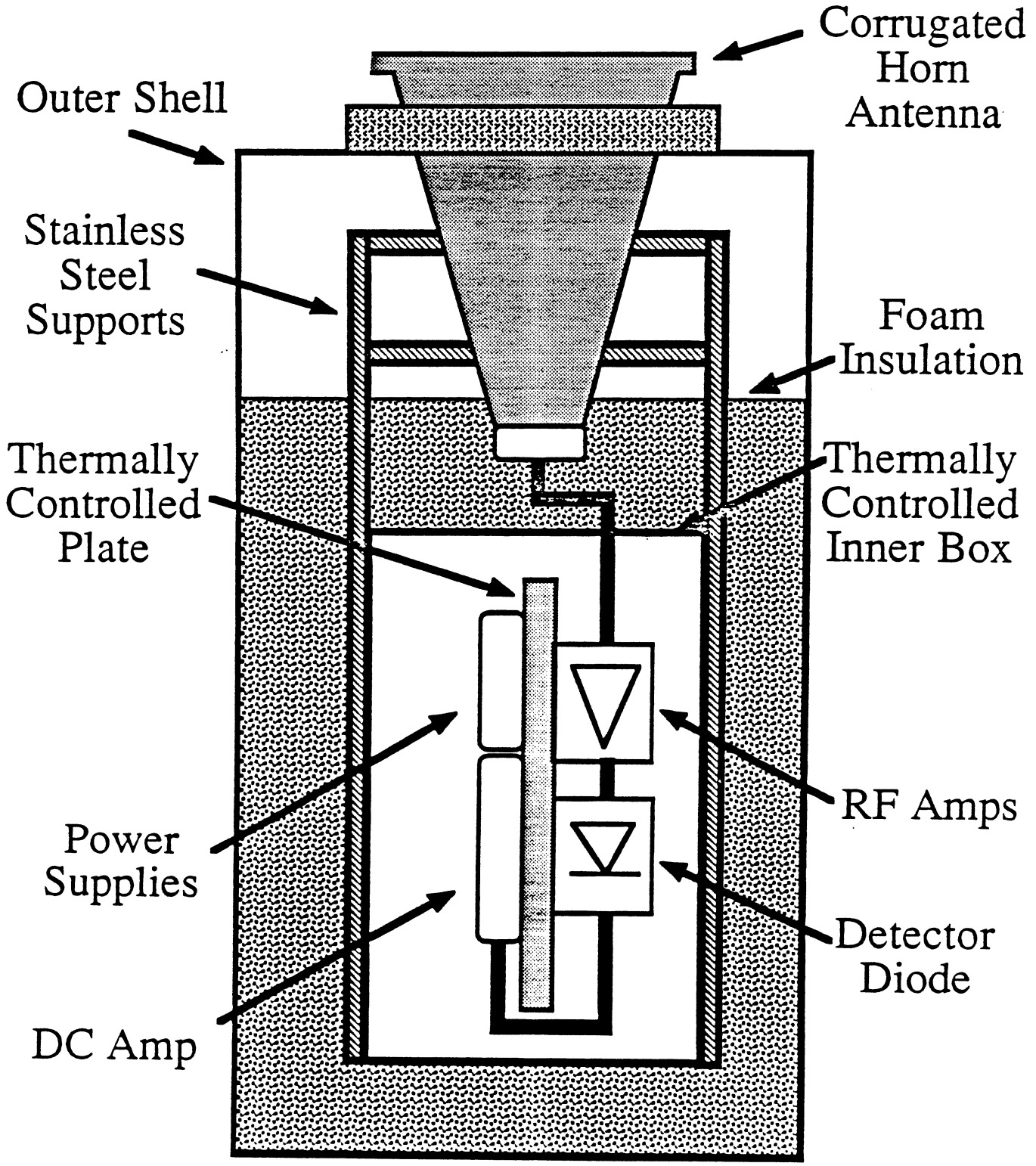
Corrugated
Horn
Antenna
Outer Shell
Stainless
Steel
Supports
Foam
Insulation
Thermally
Controlled
Plate
Thermally
Controlled
Inner Box
RF Amps
Power
Supplies
Detector
Diode
DC Amp

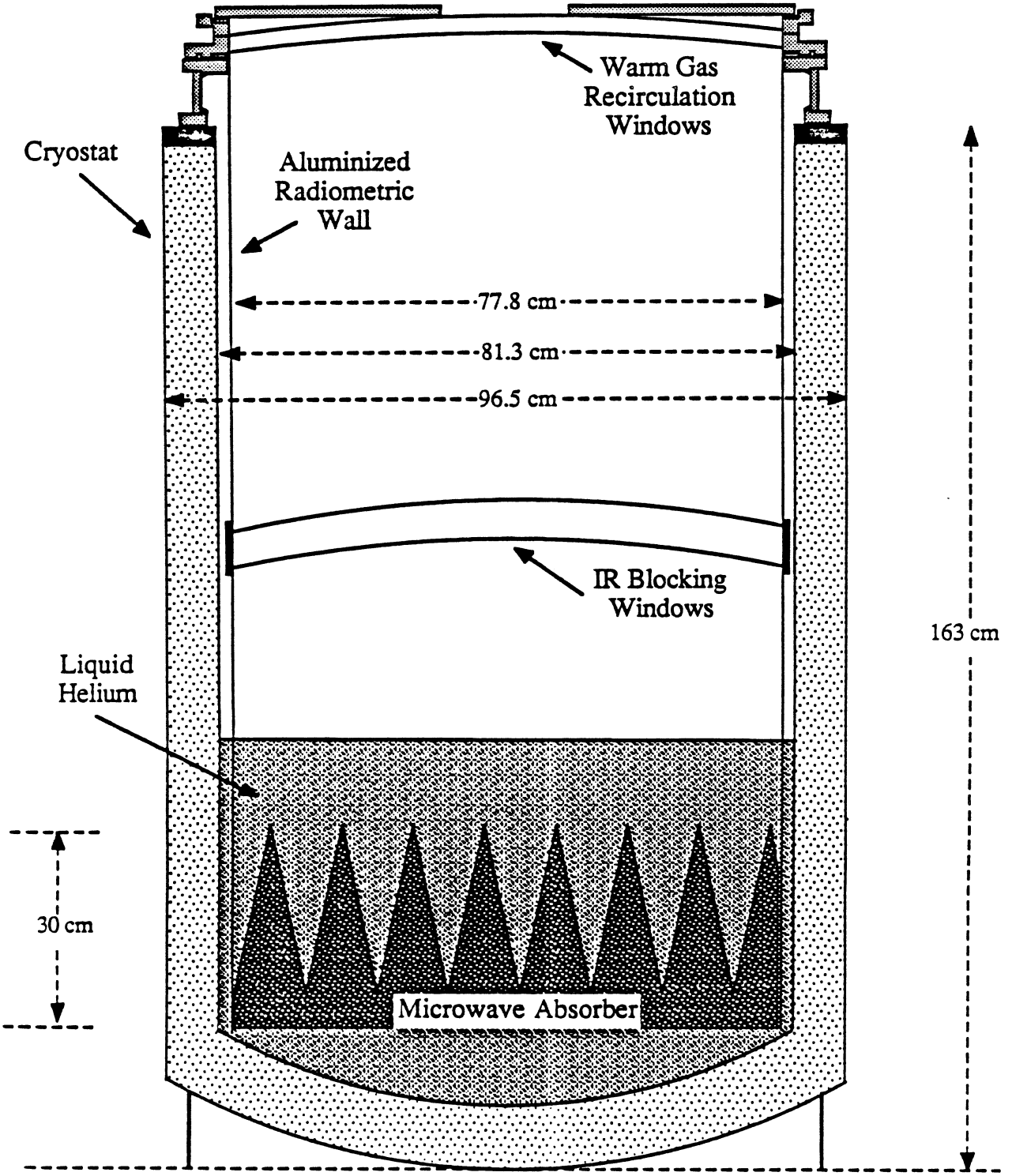
Warm Gas
Recirculation
Windows
Cryostat
Aluminized
Radiometric
Wall
77.8 cm
81.3 cm
96.5 cm
IR Blocking
Windows
163 cm
Liquid
Helium
30 cm
Microwave Absorber

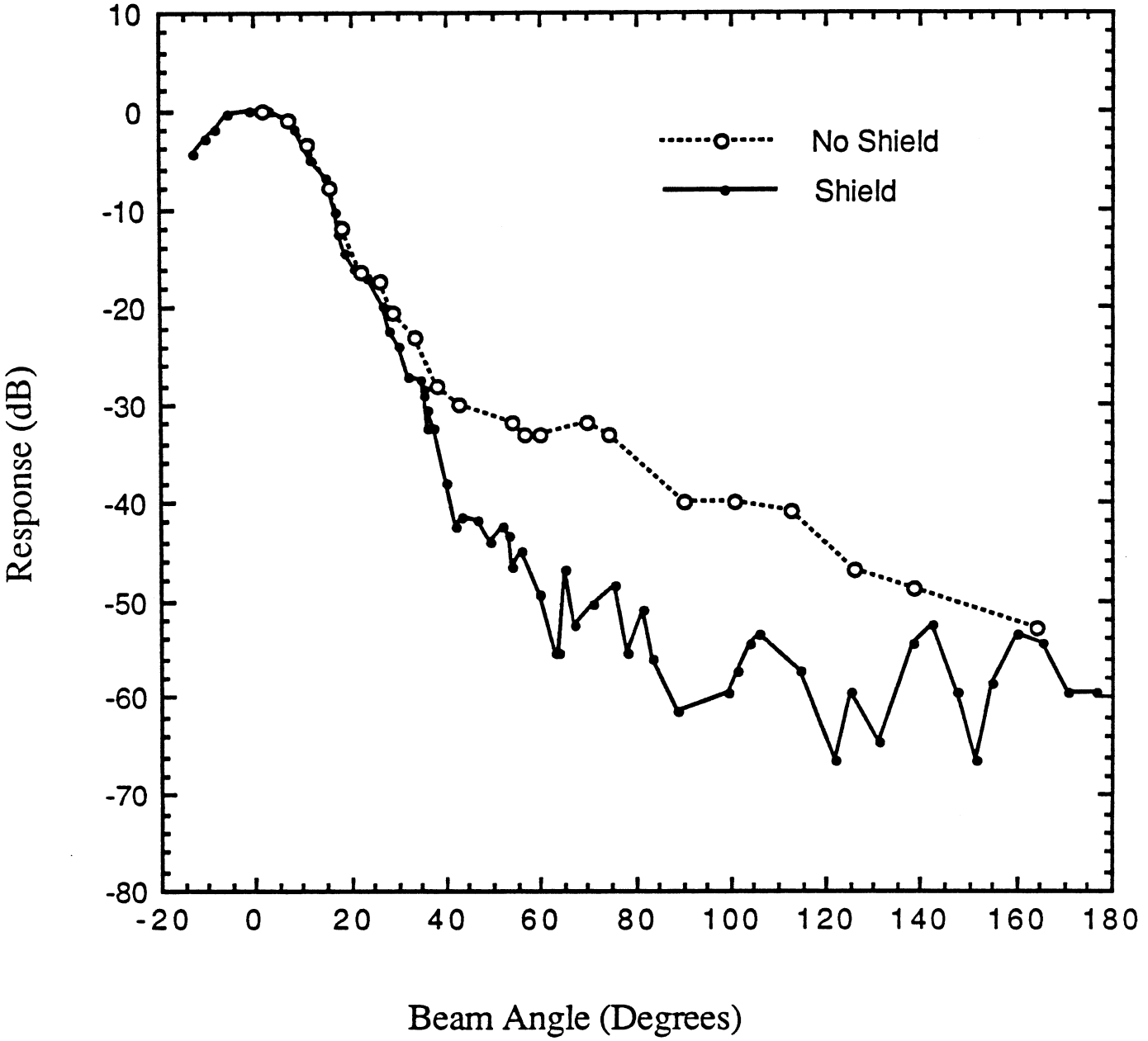
10
0
-10
-20
-30
-40
-50
-60
-70
-80
-20
0
20
40
60
80
100
120
140
160
180
No Shield
Shield
Response (dB)
Beam Angle (Degrees)

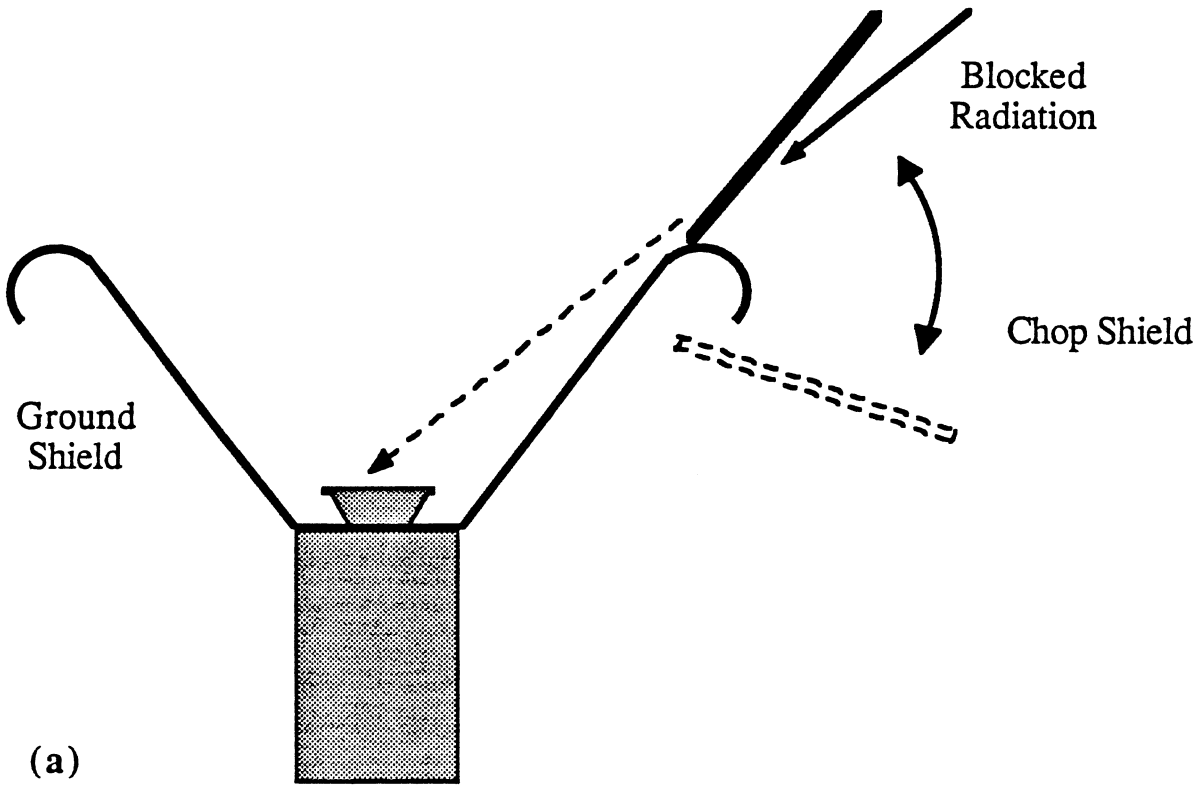
Blocked
Radiation
Chop Shield
Ground
Shield
(a)

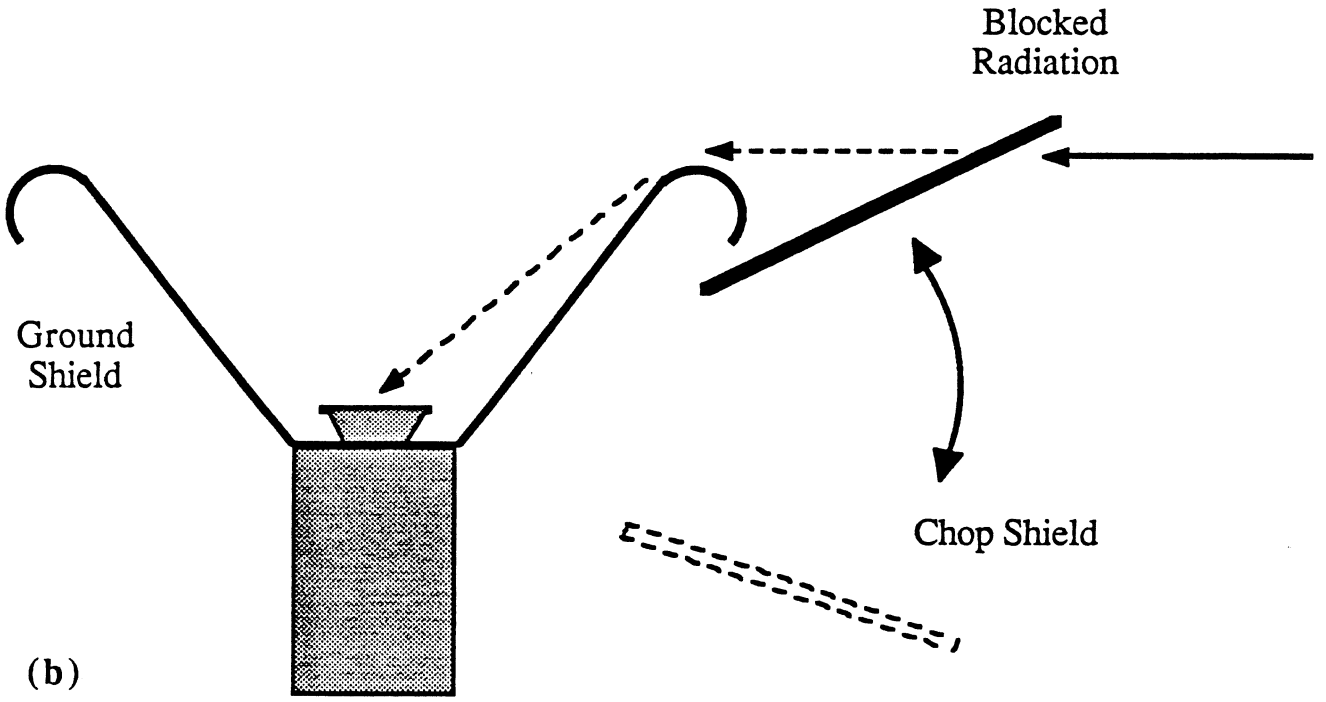
Blocked
Radiation
Ground
Shield
Chop Shield
(b)

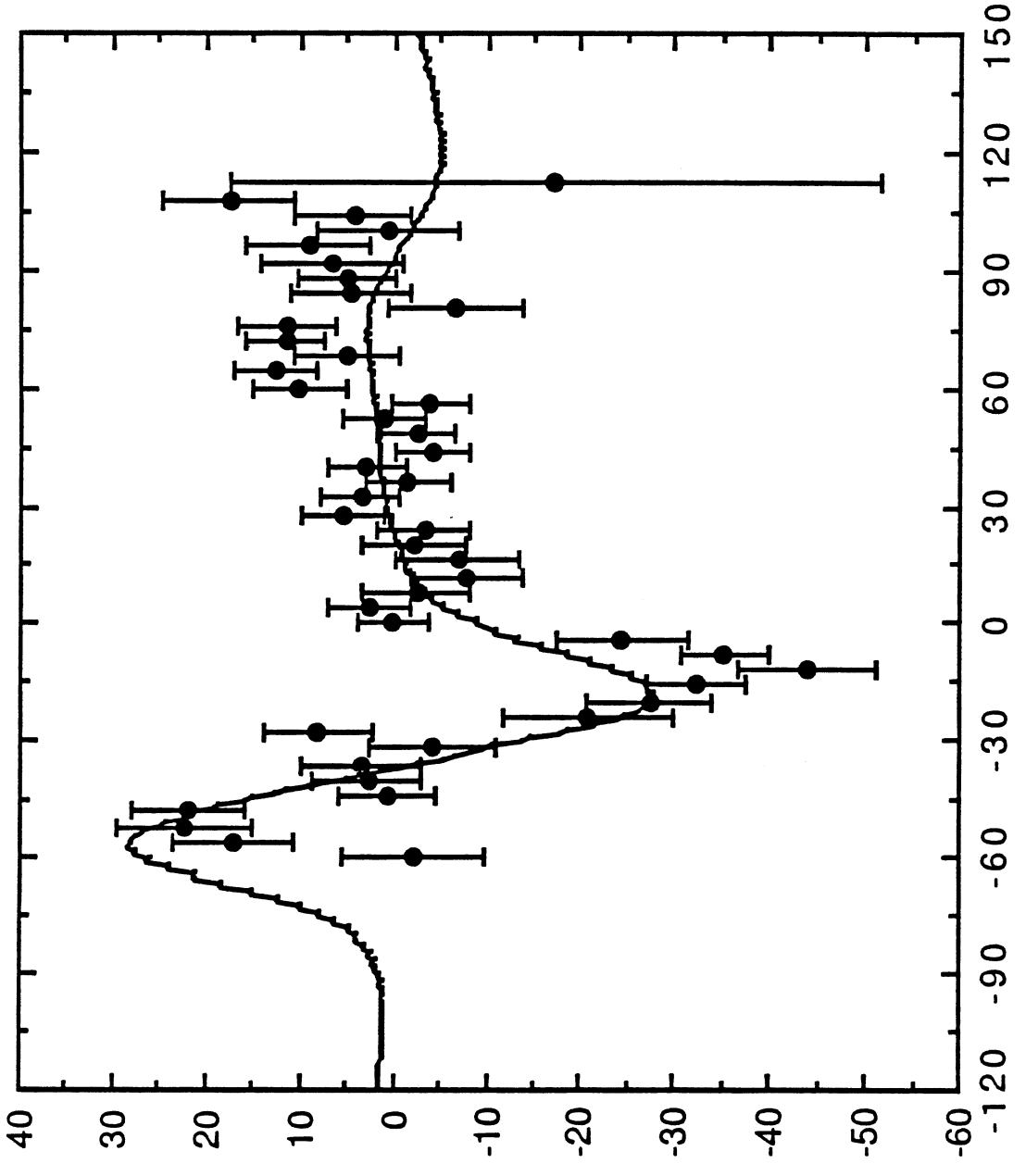
Antenna Temperature (mK)
40
30
20
10
0
-10
-20
-30
-40
-50
-60
-120
-90
-60
-30
0
30
60
90
120
150
Right Ascension (degrees)

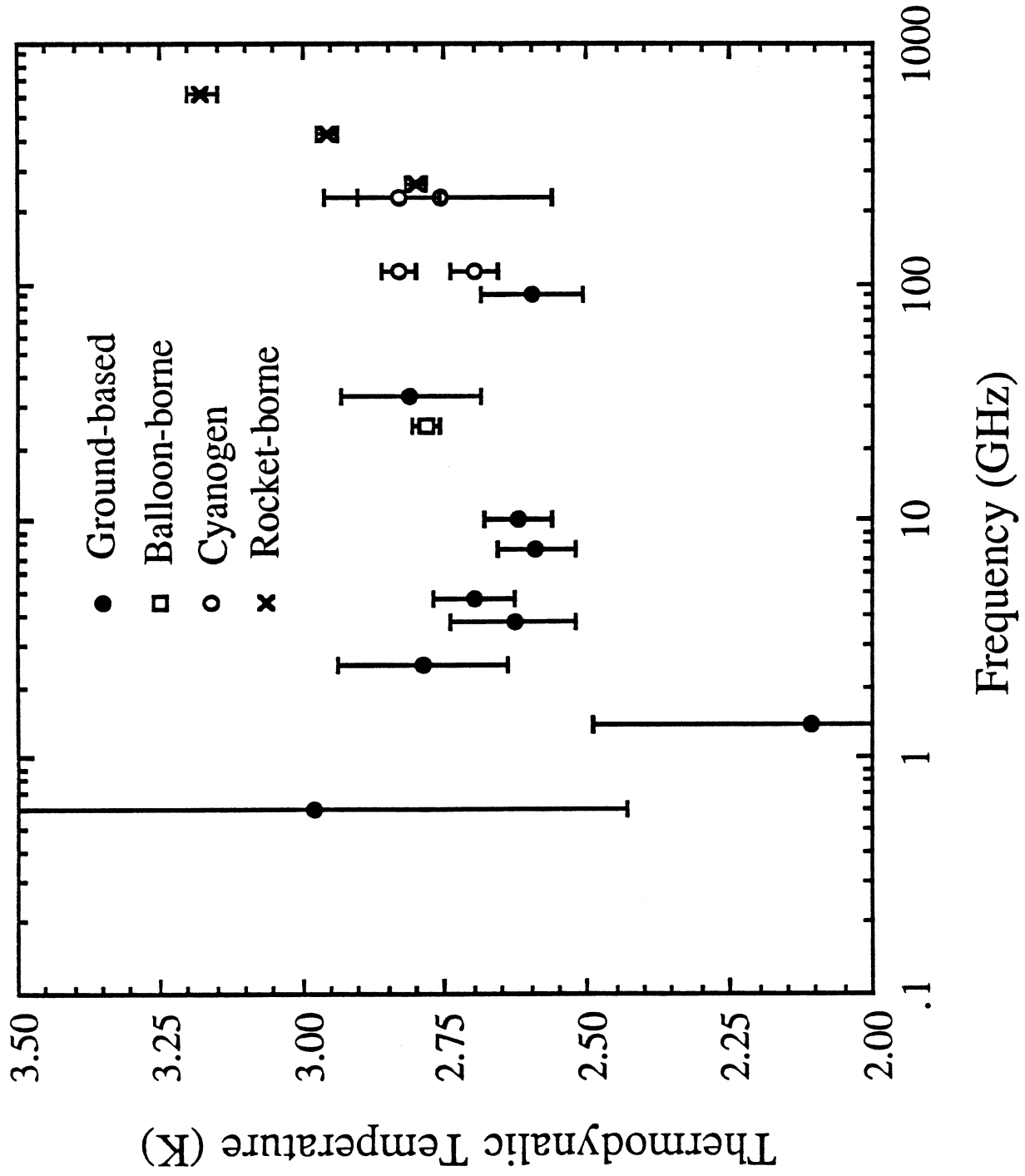
Thermodynamic Temperature (K)
3.50
3.25
3.00
2.75
2.50
2.25
2.00
.1
1
10
100
1000
Frequency (GHz)
Ground-based
Balloon-borne
Cyanogen
Rocket-borne